NANO LETTERS
Letter
Cite This: Nano Lett. 2018, 18, 5709−5715
pubs.acs.org/NanoLett

Dynamics and Spin-Valley Locking Effects in Monolayer Transition Metal Dichalcogenides

Christopher J. Ciccarino,[†,‡] Thomas Christensen,[§] Ravishankar Sundararaman,[∥] and Prineha Narang*[,†]

[†]John A. Paulson School of Engineering and Applied Sciences, Harvard University, Cambridge, Massachusetts, United States
[‡]Department of Chemistry and Chemical Biology, Harvard University, Cambridge, Massachusetts, United States
[§]Department of Physics, Massachusetts Institute of Technology, Cambridge, Massachusetts, United States
[∥]Department of Materials Science and Engineering, Rensselaer Polytechnic Institute, Troy, New York, United States

Supporting Information

ABSTRACT: Transition metal dichalcogenides have been the primary materials of interest in the field of valleytronics for their potential in information storage, yet the limiting factor has been achieving long valley decoherence times. We explore the dynamics of four monolayer TMDCs (MoS_2, $MoSe_2$, WS_2, WSe_2) using *ab initio* calculations to describe electron−electron and electron−phonon interactions. By comparing calculations which both omit and include relativistic effects, we isolate the impact of spin-resolved spin−orbit coupling on transport properties. In our work, we find that spin−orbit coupling increases carrier lifetimes at the valence band edge by an order of magnitude due to spin-valley locking, with a proportional increase in the hole mobility at room temperature. At temperatures of 50 K, we find intervalley scattering times on the order of 100 ps, with a maximum value of ∼140 ps in WSe_2. Finally, we calculate excited-carrier generation profiles which indicate that direct transitions dominate across optical energies, even for WSe_2 which has an indirect band gap. Our results highlight the intriguing interplay between spin and valley degrees of freedom critical for valleytronic applications. Further, our work points toward interesting quantum properties on-demand in transition metal dichalcogenides that could be leveraged via driving spin, valley, and phonon degrees of freedom.

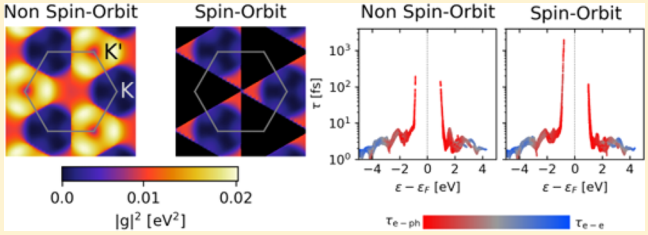

KEYWORDS: *Valleytronics, carrier dynamics, transition metal dichalcogenides, spin-valley locking*

Transition metal dichalcogenides (TMDCs) represent a class of semiconducting 2D materials of significant scientific potential.[1] Specifically, TMDCs are a key player in the fields of spintronics[2−4] and valleytronics[5,6] which seek to use degrees of freedom beyond charge to accelerate electronic computing and information processing. These materials offer quantum properties on-demand[7,8] with interesting possibilities to create topological states and nonequilibrium matter through driven phonon states.[9,10] Monolayer TMDCs are furnished with inequivalent valleys at the K and K′ points of the Brillouin zone,[11] due to the absence of an in-plane inversion center. As a result, carriers in the K and K′ valleys acquire an additional quantum number known as their valley index or valley pseudospin. Heavy transition metal atoms in these materials introduce strong spin−orbit coupling, with large spin-splitting of opposite signs at the K and K′ valleys near the band edges, leading to spin-valley coupling.[11−14] Consequently, scattering of charge carriers between valleys necessitates a simultaneous spin flip in addition to a large momentum transfer (K ↔ K′) and is therefore expected to be a slow process.[15,16]

In the current state-of-the-art in valley physics, specific valleys can be targeted and selectively populated via polarized light[17,18] and magnetic fields.[19−21] These methods for breaking valley degeneracy have now been well-explored, and a central limit in valleytronics remains the valley polarization lifetime which directly determines the retention time of information represented by the valley state.[22]

Quantifying valley polarization times in monolayer TMDCs has been led by experimental investigation,[12,15,23−26] while theoretical work has come along only recently.[27] Difficulties in quantifying valley polarization times are clear from the wide range (from picoseconds to nanoseconds) of reported lifetimes. Experimentally, 2D materials are difficult to isolate from the environment and thus determining their intrinsic properties is challenging. Substrate-based studies may suffer from unknown substrate interactions, while free-standing layers can have altered electrical properties as a result of ripples.[28,29] Outside of general experimental difficulties in 2D materials, one reason for such a discrepancy in the valley polarization times is the role of multiparticle excitations including excitons and trions. Excitons have large binding energies due to ineffective dielectric screening in 2D materials, which

Received: June 6, 2018
Revised: July 31, 2018
Published: August 1, 2018

DOI: 10.1021/acs.nanolett.8b02300
Nano Lett. 2018, 18, 5709−5715

complicates valley population mechanisms based on optical excitation. The difference between exciton valley dynamics and free electron or hole valley dynamics is significant. While exciton valley lifetimes are expected to be short, individual electron and hole lifetimes are expected to be considerably longer, and therefore represent the best candidates for effective information storage.[13]

The potential for valleytronic applications is particularly enhanced by strong spin−orbit coupling at the band edges of heavy-metal monolayer TMDCs including MoS_2, $MoSe_2$, WS_2, and WSe_2. The valence band splitting is primarily due to d_{xy} and $d_{x^2-y^2}$ orbitals of the transition metal, with splits ranging up to 0.5 eV for the heavier tungsten monolayers.[30−33] The conduction band split is significantly smaller, as this band is mostly composed of d orbitals with magnetic quantum number $m = 0$. This small conduction band split means that the inequivalent K and K′ valleys are susceptible to intervalley scattering.[27] The larger splitting of the valence band therefore makes this edge much more attractive for valleytronic applications. The exact role of spin−orbit coupling in carrier lifetimes and mobilities is, however, not yet known unambiguously.

In this manuscript, we investigate valley physics and transport properties of TMDCs using an *ab initio* framework, fully including the impact of electron−electron and electron−phonon interactions, and self-consistent spin−orbit coupling. We compare these results to spin degenerate, nonrelativistic calculations, enabling us to quantify the crucial impact of spin−orbit coupling in increasing the valence band lifetimes near the K and K′ points and the corresponding hole mobilities. In particular, we show that the large spin−orbit coupling precludes intervalley scattering near the valence band edge, increasing carrier lifetimes and mobilities by an order of magnitude. We also predict energy distributions of carriers excited upon optical absorption and find that they are dominated by direct transitions rather than indirect phonon-assisted transitions for all relevant photon energies.

We start with first-principles electronic structure calculations of the four TMDC monolayers considered here, sulfides and selenides of tungsten and molybdenum, all of which adopt the hexagonal crystal structure illustrated in Figure 1. Corresponding electronic band structures and densities of states are shown in Figure 1d−g. We find that WSe_2 is predicted to have an indirect gap, with its conduction band edge at the Q point rather than the K point (see Figure 1c), consistent with experimental findings,[34,35] while the remaining three materials have a direct gap at the K point. All materials are mechanically stable, as indicated by no imaginary frequencies in the calculated phonon band structures (see the Supporting Information).

Next, we use first-principles calculations of electron−electron and electron−phonon scattering rates to predict the net carrier lifetimes, shown as a function of carrier energy in Figure 2. The relative contributions of the two scattering mechanisms to the total scattering rate, $\tau_{kn}^{-1} = (\tau_{kn}^{e-e})^{-1} + (\tau_{kn}^{e-ph})^{-1}$, are shown using the color scale. Electron−phonon scattering (red) dominates the net scattering near the band edges, while electron−electron scattering picks up further from the band edges due to a quadratically increasing phase space for scattering. The scattering times near the band edges are the longest, because the phase space for electron−phonon scattering is proportional to the density of states near the carrier energy, which vanishes at the band edges.

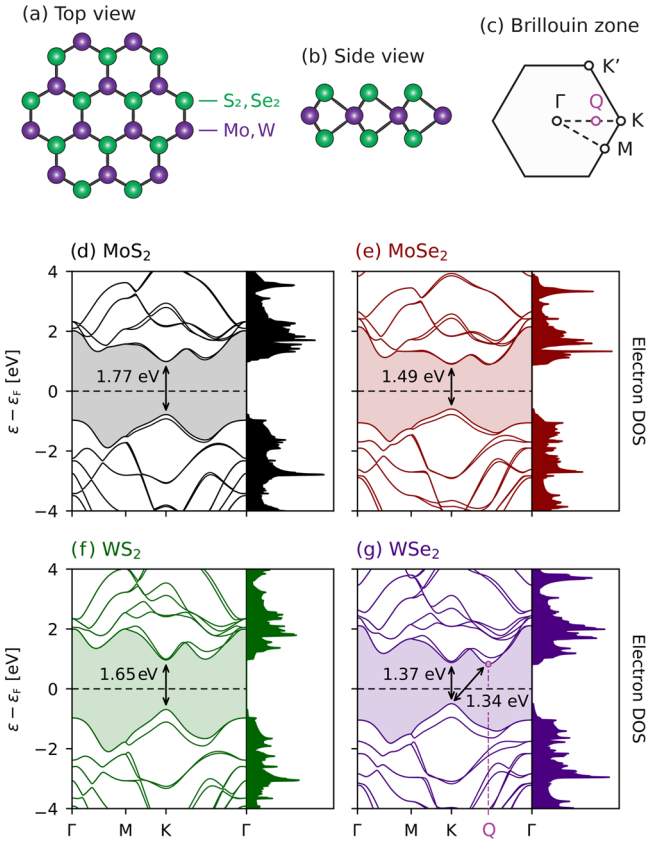

Figure 1. Monolayer TMDC structure and electronic band structure. (a, b) TMDC crystal structure and (c) corresponding Brillouin zone. The K and K′ points are energetically degenerate but inequivalent due to the lack of an inversion center. (d−g) Calculated electronic band structure and density of states for each monolayer, with band gaps annotated. Three of the four monolayers are predicted to be direct band gap semiconductors, except for WSe_2 which is predicted to have an indirect band gap with the conduction edge at the Q point, consistent with experiment.[34,35]

Overall, in Figure 2, the predicted scattering times with and without spin−orbit coupling are qualitatively similar throughout, and quantitatively similar far from the band edges. However, especially near the valence band edge, spin−orbit coupling dramatically alters the electron−phonon scattering rate, increasing the net hole lifetime by about an order of magnitude in all four monolayers. At room temperature (298 K), maximum hole lifetimes in MoS_2 and $MoSe_2$ are ∼2 ps, while they exceed 4 ps in the tungsten TMDCs.

To understand the reason for lifetime enhancement due to spin−orbit coupling, Figure 3 shows the calculated electron−phonon matrix elements (squared and summed over all phonon modes) connecting a state at the valence band edge at the K point of the Brillouin zone (BZ) with the highest valence band states at all other points of the BZ. Note that, without spin−orbit coupling, the results are 6-fold symmetric and there is strong electron−phonon coupling between the K and K′ points, which are inequivalent due to the absence of inversion symmetry. In this case, there are two degenerate spin states at each of the K and K′ valleys, and phonons strongly couple the states with the same spin. Since these are at the same energy, these states are accessible for electron−phonon scattering and result in intervalley scattering which limits the lifetime(s) of the carriers.

DOI: 10.1021/acs.nanolett.8b02300
Nano Lett. 2018, 18, 5709−5715

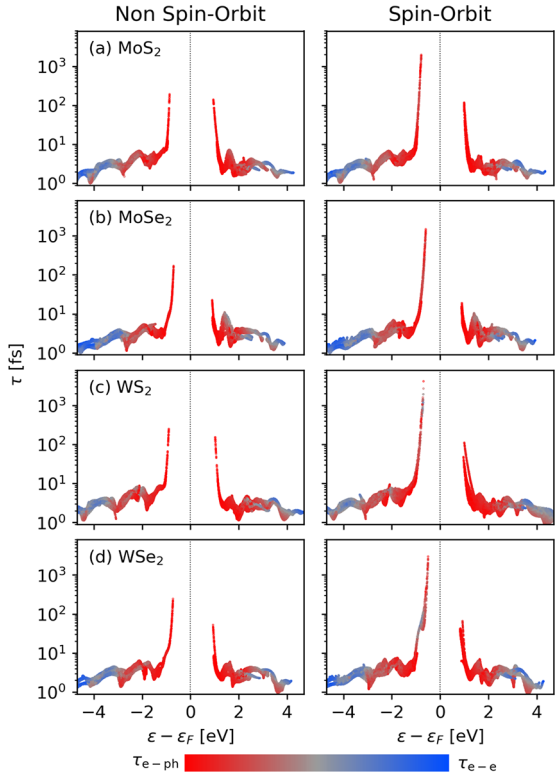

Figure 2. Total scattering lifetimes for hot carriers near the Fermi level for each of the four monolayer TMDCs (T = 298 K). Calculations are performed with (right) and without (left) spin−orbit coupling. The color bar indicates the relative contributions to scattering from electron−phonon (red) and electron−electron (blue) interactions. Lifetimes are enhanced by over an order of magnitude at the valence band edge when spin−orbit effects are considered for each monolayer, due to spin-valley locking.

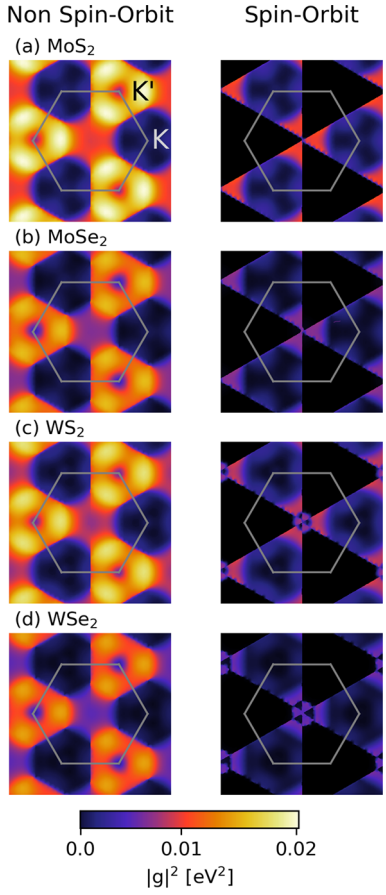

Figure 3. Electron−phonon coupling for valence-band-edge carriers in each of the monolayer TMDCs. Electron−phonon matrix element squared and summed over phonon modes, between the valence-band edge state at the K point and the highest valence band state for each wavevector **k** in the Brillouin zone (BZ), both with and without spin−orbit coupling for each of the four monolayer TMDCs. Without spin−orbit coupling, the matrix element is mostly nonzero throughout the BZ, while, with spin−orbit coupling, half of the BZ goes dark with essentially zero electron−phonon coupling to the highest occupied band. This is because these transitions would involve final electronic states with opposite spin. The strong spin−orbit splitting causes these states to be inaccessible via electron−phonon interactions. This results in spin-valley locking and much higher carrier lifetimes.

Spin−orbit coupling completely changes this picture, as shown in Figure 3. The two spin states in each of the K and K′ valleys are no longer degenerate, and the energy split occurs in the *opposite* direction at the two valleys. Consequently, the valence band edges at the K and K′ points have opposite spins, and the intervalley scattering between these equal energy states must involve a spin flip,[13] which has an extremely small matrix element. This manifests in Figure 3, as an entire half of the BZ centered on the intervalley scattering process has an essentially zero electron−phonon matrix element. The phonon states which coupled the spin-degenerate electronic states in the case without spin−orbit coupling have now been split away to an energy inaccessible at room temperature for electron−phonon scattering. This forces the carriers of a given spin to remain locked to a given valley, and this spin-valley locking produces the sharp increase in the electron−phonon lifetime of holes near the valence band edge for all four TMDCs in Figure 2. On the other hand, the spin−orbit split at the conduction band edge is negligible and there is hence no electron lifetime enhancement compared to the non-spin−orbit case.

As shown above, the rate of intervalley scattering determines the valence-band-edge carrier lifetimes. These carrier lifetimes are therefore the time for which holes remain locked to a valley, effectively the retention time of valley information in valleytronic devices. Despite a number of experimental investigations using a variety of methods, the valley retention times have not yet been conclusively determined. Using exactly the same first-principles methodology as above, we also calculate the band-edge hole lifetimes at T = 50 K, where the lifetimes are expected to be longer (and more useful for valleytronics) due to the lowered phase space for scattering. We find the valley retention time to be 57 and 67 ps for MoS_2 and $MoSe_2$ and 62 and 138 ps for WS_2 and WSe_2. The relative lifetime values among the four monolayers correlate with the strength of the electron−phonon coupling seen in Figure 3. This lifetime trend also correlates with the predicted energy difference between the Γ and K valleys at the valence edge.

The methods used to calculate these lifetimes only capture processes in an atomically perfect crystal, ignoring potential interactions with defects and substrates, and therefore represent a best-case scenario for monolayer TMDC valley lifetimes. Unambiguous experimental determination of the limiting valley retention times is challenging precisely because it is impossible to disentangle substrate interactions and dopant/defect effects. Additionally, excitonic and other multiparticle effects complicate signatures from optical

DOI: 10.1021/acs.nanolett.8b02300
Nano Lett. 2018, 18, 5709−5715

measurements, all of which we exclude in our theoretical predictions above. Consequently, we predict the best-case valley lifetime in monolayer TMDCs at 50 K to exceed the 100 ps scale for WSe_2 and to be roughly on the same order of magnitude for the others.

The enhancement of band-edge carrier lifetimes due to suppression of intervalley scattering should result in a corresponding increase in the carrier mobility due to spin−orbit coupling (since mobility $\mu = e\tau/m^* \propto \tau$ in Drude theory). Figure 4 shows the intrinsic carrier mobility due to electron−

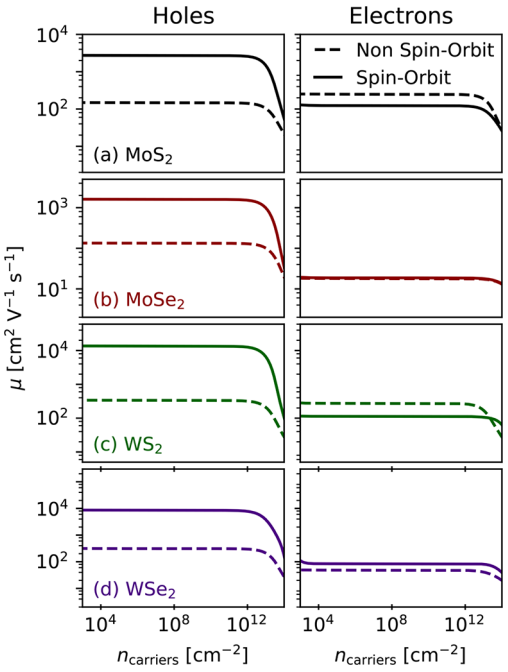

Figure 4. Hole and electron mobility versus carrier density at $T = 298$ K for each of the monolayer TMDCs. Hole mobility is enhanced by spin-valley locking by over an order of magnitude across all four TMDCs in the calculations including spin−orbit coupling, compared to those that do not include it. The corresponding effect on electron mobility is less pronounced, where instead lowering of the Q valley in the spin−orbit calculations introduces low-energy scattering and decreases the mobility. WSe_2 is an exception where the Q point is sufficiently isolated from K at the conduction edge, such that this scattering is suppressed and the electron mobility increases.

phonon scattering as a function of carrier density, both for electrons and holes, with and without spin−orbit coupling. As expected, the hole mobility is enhanced by over an order of magnitude when spin−orbit coupling is considered, exactly as was the case for carrier lifetimes. Previous theoretical predictions of hole mobilities in these materials[36−39] are all below 1000 $cm^2\ V^{-1}\ s^{-1}$ because they do not include spin−orbit interactions; our nonrelativistic calculations are in good agreement with these previous studies. The trend in hole mobility is consistent with the corresponding lifetimes, with the largest hole mobility in $WS_2 \sim 10^4\ cm^2\ V^{-1}\ s^{-1}$.

On the other hand, electron mobility is less drastically affected by spin−orbit coupling. The differences can be explained on the basis of the band structures calculated with and without spin−orbit coupling. In the spin−orbit case, the conduction band edge is found to be nearly degenerate between the K and Q points (see Figure 1). This introduces low-energy scattering between these two valleys. Meanwhile, nonrelativistic calculations find the K and Q valleys are more energetically separated, making intervalley scattering via phonons less accessible. Consequently, electron mobility is predicted to decrease due to spin−orbit coupling for some TMDCs, as shown in Figure 4. However, in the case of WSe_2, the energy difference between the K and Q conduction valleys is larger, and spin−orbit coupling increases the electron mobilities instead. The overall differences in mobilities due to spin−orbit effects are smaller for electrons as compared to holes. This is also visible in comparing the lifetimes at the conduction and valence edges in Figure 2.

Experimentally measured mobilities in monolayer TMDCs are smaller than theoretical predictions due to several inherent nonidealities including substrate effects, trapped impurities, airborne adsorbates, and overall sample quality including defects and grain size.[40,41] Our predictions shed light on the underlying physics of carrier lifetimes and transport in 2D TMDCs, underscoring the importance of spin-valley locking not just in valleytronics but also in overall charge transport for electronic applications such as in field-effect transistors.

We further investigate the dynamics of these systems by determining the nature of hot carrier generation. We capture the energy distributions of carriers that are excited upon optical absorption by accounting for both direct and phonon-assisted transitions using our previously established first-principles methodology.[42−49] Figure 5 shows that direct

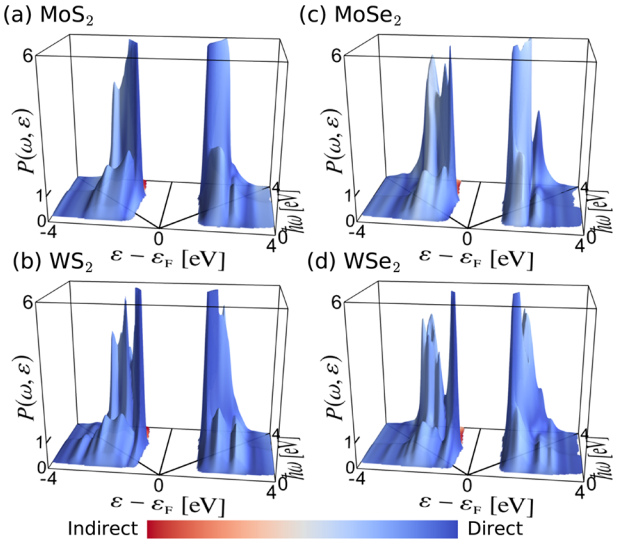

Figure 5. Hot carrier energy distributions $P(\omega, \varepsilon)$ as a function of optical excitation energy $\hbar\omega$ and relative carrier energy $\varepsilon - \varepsilon_F$ for each of the four monolayer TMDCs. The distribution at each photon energy is normalized such that a flat distribution would yield 1, while the color scale indicates the contribution from direct and phonon-assisted processes. Direct transitions dominate hot carrier generation for each of these monolayers, even in the case of the (slightly) indirect-gapped WSe_2.

transitions dominate carrier generation in all of these materials, as expected for direct gap semiconductors where the band gap and optical gap are equal so that direct transitions are always allowed. However, this is also the case for the indirect-gap WSe_2 because the small energy difference of the conduction band edges at the K and Q points results in a small difference between the band gap and optical gap, making it behave essentially as a direct band gap semiconductor.

DOI: 10.1021/acs.nanolett.8b02300
Nano Lett. 2018, 18, 5709−5715

We use first-principles calculations of carrier dynamics in monolayer TMDCs with an *ab initio* treatment of electron−electron and electron−phonon interactions to elucidate the critical effect of spin−orbit coupling in these materials. Our results highlight the importance of spin-valley locking of holes near the valence band edge at the K and K′ points, a consequence of spin−orbit coupling, on carrier lifetimes, valley retention time, and charge transport. In particular, we find that spin−orbit coupling enhances the hole lifetimes and mobilities by an order of magnitude in all four materials considered here. Electron lifetimes and mobilities are less affected in comparison, due to much smaller spin−orbit coupling effects near the conduction band edge. We predict the ideal valley relaxation time in these materials at a lower temperature of 50 K to be at the 100 ps scale, with the largest value for WSe_2 ∼ 140 ps exceeding the others by about a factor of 2. While our results focus on monolayer systems, multilayer and heterostructured TMDC systems with strong spin−orbit coupling should also have similar spin-valley locking physics, which necessitates a careful analysis of the intervalley scattering mechanisms, fully accounting for the effect of phonons from a self-consistent spin−orbit coupling perspective.

We used the open-source JDFTx density-functional theory software for structural relaxation, electronic band structure, phonon, and electron−phonon matrix element calculations.[50] We carried out all calculations each with relativistic and nonrelativistic ultrasoft pseudopotentials[51] to investigate the effect of spin−orbit coupling. For the exchange-correlation functional, we used the PBEsol generalized-gradient approximation,[52] which yielded relaxed lattice constants within 1% of experimental values. To eliminate the effect of periodic images in the out-of-plane direction, we used truncated Coulomb interactions throughout for these 2D materials.[53]

All electronic calculations employed a 18 × 18 × 1 Γ-centered **k**-point mesh for BZ sampling with a plane-wave energy cutoff of 30 hartree. Phonon properties were calculated from symmetry-irreducible perturbations in a 6 × 6 × 1 supercell both with and without self-consistent spin−orbit coupling via the frozen phonon approach within the harmonic approximation. Directly calculating electron−phonon scattering properties in DFT both with and without self-consistent spin−orbit coupling is expensive due to the energy mismatch between electron and phonon scales necessitating extremely fine BZ sampling. Consequently, we convert all electron, phonon, and electron−phonon properties calculated at the above "coarse" BZ meshes to a basis of maximally localized Wannier functions[54] (starting from transition metal d and chalcogen p trial orbitals). We then interpolate these properties[42,55] to substantially finer electron k and phonon q meshes with ∼1000 points per dimension (∼10^6 total), used for all carrier scattering and optical response properties described below.

The total carrier lifetime is determined by electron−electron and electron−phonon scattering, with the total scattering rate given by Matthiessen's rule

$$\tau_{\mathbf{k}n}^{-1} = (\tau_{\mathbf{k}n}^{\mathrm{e-e}})^{-1} + (\tau_{\mathbf{k}n}^{\mathrm{e-ph}})^{-1} \tag{1}$$

for electrons of each band n at wavevector $\mathbf{k}$ in the two-dimensional BZ. The electron−electron scattering rate is calculated from the imaginary part of the carrier self-energy, given by[42,56]

$$(\tau_{\mathbf{k}n}^{\mathrm{e-e}})^{-1} = \frac{2\pi}{\hbar}\int_{\mathrm{BZ}}\frac{\mathrm{d}\mathbf{k}'}{(2\pi)^2}\sum_{n'}\sum_{\mathbf{G}\mathbf{G}'}\tilde{\rho}_{\mathbf{k}'n',\mathbf{k}n}(\mathbf{G})\tilde{\rho}^{*}_{\mathbf{k}'n',\mathbf{k}n}(\mathbf{G}') \times \frac{1}{\pi}\,\mathrm{Im}\,W_{\mathbf{G}\mathbf{G}'}(\mathbf{k}'-\mathbf{k},\,\varepsilon_{\mathbf{k}n}-\varepsilon_{\mathbf{k}'n'}) \tag{2}$$

The above expression is essentially the imaginary part of the interaction of the one-particle electronic density matrices $\tilde{\rho}_{\mathbf{k}'n',\mathbf{k}n}(\mathbf{G})$ through the dynamically screened Coulomb interaction, $W_{\mathbf{G}\mathbf{G}'}(\mathbf{k}'-\mathbf{k},\,\omega)$, evaluated within the random phase approximation. This calculation is performed directly in the plane-wave basis of reciprocal lattice vectors $\mathbf{G}$ and $\mathbf{G}'$ and involves a sum over a full second set of electronic states $(\mathbf{k}'n')$. See ref 42 for further details.

We calculate the electron−phonon scattering rate using Fermi's golden rule[42]

$$(\tau_{\mathbf{k}n}^{\mathrm{e-ph}})^{-1} = \frac{2\pi}{\hbar}\sum_{n'\alpha\pm}\int_{\mathrm{BZ}}\frac{\Omega\mathrm{d}\mathbf{k}'}{(2\pi)^2}\delta(\varepsilon_{\mathbf{k}'n'}-\varepsilon_{\mathbf{k}n}\mp\hbar\omega_{\mathbf{q}\alpha}) \times\left[n_{\mathbf{q}\alpha}+\frac{1}{2}\mp\left(\frac{1}{2}-f_{\mathbf{k}'n'}\right)\right]|g^{\mathbf{q}\alpha}_{\mathbf{k}'n',\mathbf{k}n}|^2 \tag{3}$$

where $\varepsilon_{\mathbf{k}n}$ and $f_{\mathbf{k}n}$ are energies and Fermi occupations of electrons at wavevector $\mathbf{k}$ in band n, $\omega_{\mathbf{q}\alpha}$ and $n_{\mathbf{q}\alpha}$ are angular frequencies and Bose occupations of phonons at wavevector $\mathbf{q}$ with polarization index α, and $g^{\mathbf{q}\alpha}_{\mathbf{k}'n',\mathbf{k}n}$ is the electron−phonon matrix element coupling them to the final electronic state $(\mathbf{k}'n')$ (a three-vertex in the diagrammatic picture) with $\mathbf{q} = \mathbf{k}' - \mathbf{k}$ by momentum conservation. Above, the summation over ± accounts for phonon emission and absorption processes.

For calculating carrier mobilities, we first evaluate carrier momentum relaxation times due to electron−phonon scattering

$$(\tau_{\mathbf{k}n}^{p})^{-1} = \frac{2\pi}{\hbar}\sum_{n'\alpha\pm}\int_{\mathrm{BZ}}\frac{\Omega\mathrm{d}\mathbf{k}'}{(2\pi)^2}\delta(\varepsilon_{\mathbf{k}'n'}-\varepsilon_{\mathbf{k}n}\mp\hbar\omega_{\mathbf{q}\alpha}) \times\left[n_{\mathbf{q}\alpha}+\frac{1}{2}\mp\left(\frac{1}{2}-f_{\mathbf{k}'n'}\right)\right]|g^{\mathbf{q}\alpha}_{\mathbf{k}'n',\mathbf{k}n}|^2 \times\left(1-\frac{\mathbf{v}_{\mathbf{k}n}\cdot\mathbf{v}_{\mathbf{k}'n'}}{|\mathbf{v}_{\mathbf{k}n}||\mathbf{v}_{\mathbf{k}'n'}|}\right) \tag{4}$$

which is identical to eq 3 except for an additional final factor accounting for the scattering angle between initial and final electron band velocities $\mathbf{v}_{\mathbf{k}n}$ (defined by $\mathbf{v} \equiv \partial\varepsilon/\partial\mathbf{k}$). Then, we calculate the mobility by solving the linearized Boltzmann equation using a full-band relaxation-time approximation[42,45,57]

$$\bar{\mu}(\varepsilon_{\mathrm{F}}) = \frac{e}{|n(\varepsilon_{\mathrm{F}})|}\sum_{n}\int_{\mathrm{BZ}}\frac{g_s\mathrm{d}\mathbf{k}}{(2\pi)^2}\frac{\partial f_{\mathbf{k}n}(\varepsilon_{\mathrm{F}})}{\partial\varepsilon_{\mathbf{k}n}}(\mathbf{v}_{\mathbf{k}n}\otimes\mathbf{v}_{\mathbf{k}n})\tau^{p}_{\mathbf{k}n} \tag{5}$$

where the Fermi function derivative selects out carriers that contribute to transport at a particular doping level specified by Fermi level position ε_{F} and where g_s (=1 with and =2 without spin−orbit coupling) is the spin-degeneracy factor. Above, the Fermi-level-dependent carrier density is defined as

$$n(\varepsilon_{\mathrm{F}}) = \sum_{n}\int_{\mathrm{BZ}}\frac{g_s\mathrm{d}\mathbf{k}}{(2\pi)^2}f_{\mathbf{k}n}(\varepsilon_{\mathrm{F}}) - n_0$$

where n_0 is the number density of carriers in the neutral DFT calculation; this is positive for n-type semiconductors with a net electron density and negative for p-type semiconductors

DOI: 10.1021/acs.nanolett.8b02300
Nano Lett. 2018, 18, 5709−5715

with a net hole density. By varying the Fermi level position from near the valence band edge to near the conduction band edge, we trace out the hole mobility (when $n < 0$) and then the electron mobility (when $n > 0$) as a function of carrier density $|n|$, as shown in Figure 4.

■ ASSOCIATED CONTENT

Supporting Information

The Supporting Information is available free of charge on the ACS Publications website at DOI: 10.1021/acs.nanolett.8b02300.

Phonon dispersions for each of the monolayer TMDCs, additional details for hot carrier generation via *ab initio* calculations of the dielectric function, and expressions used to capture direct and phonon-assisted transitions (PDF)

■ AUTHOR INFORMATION

Corresponding Author

*E-mail: prineha@seas.harvard.edu. Phone: (617) 496-4710.

ORCID

Ravishankar Sundararaman: 0000-0002-0625-4592

Prineha Narang: 0000-0003-3956-4594

Notes

The authors declare no competing financial interest.

■ ACKNOWLEDGMENTS

This research used resources of the National Energy Research Scientific Computing Center, a DOE Office of Science User Facility supported by the Office of Science of the U.S. Department of Energy under Contract No. DE-AC02-05CH11231, as well as resources at the Research Computing Group at Harvard University. T.C. acknowledges support from the Danish Council for Independent Research (Grant No. DFF-6108-00667). R.S. acknowledges start-up funding from the Materials Science and Engineering department at Rensselaer Polytechnic Institute. C.C. and P.N. acknowledge support from the STC Center for Integrated Quantum Materials NSF grant number DMR-1231319, and ONR Award N00014-18-1-2691.

■ REFERENCES

(1) Kato, Y.; Myers, R. C.; Gossard, A. C.; Awschalom, D. D. *Nature* **2004**, *427*, 50.

(2) Wolf, S. A.; Awschalom, D. D.; Buhrman, R. A.; Daughton, J. M.; von Molnár, S.; Roukes, M. L.; Chtchelkanova, A. Y.; Treger, D. M. *Science* **2001**, *294*, 1488.

(3) Dankert, A.; Dash, S. P. *Nat. Commun.* **2017**, *8*, 16093.

(4) Han, W. *APL Mater.* **2016**, *4*, 032401.

(5) Ye, Y.; Xiao, J.; Wang, H.; Ye, Z.; Zhu, H.; Zhao, M.; Wang, Y.; Zhao, J.; Yin, X.; Zhang, X. *Nat. Nanotechnol.* **2016**, *11*, 598−602.

(6) Xiao, D.; Liu, G.-B.; Feng, W.; Xu, X.; Yao, W. *Phys. Rev. Lett.* **2012**, *108*, 196802.

(7) Basov, D. N.; Averitt, R. D.; Hsieh, D. *Nat. Mater.* **2017**, *16*, 1077.

(8) Chumak, A. V.; Vasyuchka, V. I.; Serga, A. A.; Hillebrands, B. *Nat. Phys.* **2015**, *11*, 453.

(9) Hübener, H.; De Giovannini, U.; Rubio, A. *Nano Lett.* **2018**, *18*, 1535−1542.

(10) Shin, D.; Hübener, H.; De Giovannini, U.; Jin, H.; Rubio, A.; Park, N. *Nat. Commun.* **2018**, *9*, No. 638.

(11) Schaibley, J. R.; Yu, H.; Clark, G.; Rivera, P.; Ross, J. S.; Seyler, K. L.; Yao, W.; Xu, X. *Nat. Rev. Mater.* **2016**, *1*, 16055.

(12) Yan, T.; Yang, S.; Li, D.; Cui, X. *Phys. Rev. B: Condens. Matter Mater. Phys.* **2017**, *95*, 241406.

(13) Xu, X.; Yao, W.; Xiao, D.; Heinz, T. F. *Nat. Phys.* **2014**, *10*, 343−350.

(14) De Giovannini, U.; Hübener, H.; Rubio, A. *Nano Lett.* **2016**, *16*, 7993−7998.

(15) Xie, L.; Cui, X. *Proc. Natl. Acad. Sci. U. S. A.* **2016**, *113*, 3746−3750.

(16) Song, Y.; Dery, H. *Phys. Rev. Lett.* **2013**, *111*, 026601.

(17) Mak, K. F.; He, K.; Shan, J.; Heinz, T. F. *Nat. Nanotechnol.* **2012**, *7*, 494−498.

(18) Zeng, H.; Dai, J.; Yao, W.; Xiao, D.; Cui, X. *Nat. Nanotechnol.* **2012**, *7*, 490−493.

(19) MacNeill, D.; Heikes, C.; Mak, K. F.; Anderson, Z.; Kormányos, A.; Zólyomi, V.; Park, J.; Ralph, D. C. *Phys. Rev. Lett.* **2015**, *114*, 037401.

(20) Aivazian, G.; Gong, Z.; Jones, A. M.; Chu, R.-L.; Yan, J.; Mandrus, D. G.; Zhang, C.; Cobden, D.; Yao, W.; Xu, X. *Nat. Phys.* **2015**, *11*, 148−152.

(21) Srivastava, A.; Sidler, M.; Allain, A. V.; Lembke, D. S.; Kis, A.; Imamoiğlu, A. *Nat. Phys.* **2015**, *11*, 141−147.

(22) Kim, J.; Jin, C.; Chen, B.; Cai, H.; Zhao, T.; Lee, P.; Kahn, S.; Watanabe, K.; Taniguchi, T.; Tongay, S.; Crommie, M. F.; Wang, F. *Sci. Adv.* **2017**, *3*, No. e1700518.

(23) Kumar, N.; He, J.; He, D.; Wang, Y.; Zhao, H. *Nanoscale* **2014**, *6*, 12690−12695.

(24) Wang, Q.; Ge, S.; Li, X.; Qiu, J.; Ji, Y.; Feng, J.; Sun, D. *ACS Nano* **2013**, *7*, 11087−11093.

(25) Mai, C.; Barrette, A.; Yu, Y.; Semenov, Y. G.; Kim, K. W.; Cao, L.; Gundogdu, K. *Nano Lett.* **2014**, *14*, 202−206.

(26) Zhu, C. R.; Zhang, K.; Glazov, M.; Urbaszek, B.; Amand, T.; Ji, Z. W.; Liu, B. L.; Marie, X. *Phys. Rev. B: Condens. Matter Mater. Phys.* **2014**, *90*, 161302.

(27) Molina-Sánchez, A.; Sangalli, D.; Wirtz, L.; Marini, A. *Nano Lett.* **2017**, *17*, 4549−4555.

(28) Brivio, J.; Alexander, D. T. L.; Kis, A. *Nano Lett.* **2011**, *11*, 5148−5153.

(29) Miró, P.; Ghorbani-Asl, M.; Heine, T. *Adv. Mater.* **2013**, *25*, 5473−5475.

(30) Zhu, Z. Y.; Cheng, Y. C.; Schwingenschlögl, U. *Phys. Rev. B: Condens. Matter Mater. Phys.* **2011**, *84*, 153402.

(31) Mak, K. F.; Lee, C.; Hone, J.; Shan, J.; Heinz, T. F. *Phys. Rev. Lett.* **2010**, *105*, 136805.

(32) Zhang, Y.; et al. *Nat. Nanotechnol.* **2013**, *9*, 111−115.

(33) Zhao, W.; Ghorannevis, Z.; Chu, L.; Toh, M.; Kloc, C.; Tan, P.-H.; Eda, G. *ACS Nano* **2013**, *7*, 791−797.

(34) Zhang, C.; Chen, Y.; Johnson, A.; Li, M.-Y.; Li, L.-J.; Mende, P. C.; Feenstra, R. M.; Shih, C.-K. *Nano Lett.* **2015**, *15*, 6494−6500.

(35) Hsu, W.-T.; Lu, L.-S.; Wang, D.; Huang, J.-K.; Li, M.-Y.; Chang, T.-R.; Chou, Y.-C.; Juang, Z.-Y.; Jeng, H.-T.; Li, L.-J.; Chang, W.-H. *Nat. Commun.* **2017**, *8*, 929.

(36) Kaasbjerg, K.; Thygesen, K. S.; Jacobsen, K. W. *Phys. Rev. B: Condens. Matter Mater. Phys.* **2012**, *85*, 115317.

(37) Li, X.; Mullen, J. T.; Jin, Z.; Borysenko, K. M.; Buongiorno Nardelli, M.; Kim, K. W. *Phys. Rev. B: Condens. Matter Mater. Phys.* **2013**, *87*, 115418.

(38) Ma, N.; Jena, D. *Phys. Rev. X* **2014**, *4*, No. 011043.

(39) Jin, Z.; Li, X.; Mullen, J. T.; Kim, K. W. *Phys. Rev. B: Condens. Matter Mater. Phys.* **2014**, *90*, 045422.

(40) Yu, Z.; Ong, Z.-Y.; Li, S.; Xu, J.-B.; Zhang, G.; Zhang, Y.-W.; Shi, Y.; Wang, X. *Adv. Funct. Mater.* **2017**, *27*, 1604093.

(41) Ahmed, S.; Yi, J. *Nano-Micro Lett.* **2017**, *9*, 50.

(42) Brown, A. M.; Sundararaman, R.; Narang, P.; Goddard, W. A.; Atwater, H. A. *ACS Nano* **2016**, *10*, 957−966.

(43) Narang, P.; Zhao, L.; Claybrook, S.; Sundararaman, R. *Adv. Opt. Mater.* **2017**, *5*, 1600914.

(44) Coulter, J.; Sundararaman, R.; Narang, P. arXiv: 1804.06310, **2018**.

DOI: 10.1021/acs.nanolett.8b02300
Nano Lett. 2018, 18, 5709−5715

(45) Habib, A.; Florio, R.; Sundararaman, R. *J. Opt.* **2018**, *20*, 064001.
(46) Papadakis, G. T.; Narang, P.; Sundararaman, R.; Rivera, N.; Buljan, H.; Engheta, N.; Soljačić, M. *ACS Photonics* **2018**, *5*, 384−389.
(47) Sundararaman, R.; Narang, P.; Jermyn, A. S.; Goddard, W. A.; Atwater, H. A. *Nat. Commun.* **2014**, *5*, 5788.
(48) Brown, A. M.; Sundararaman, R.; Narang, P.; Goddard, W. A.; Atwater, H. A. *Phys. Rev. B: Condens. Matter Mater. Phys.* **2016**, *94*, 075120.
(49) Shirodkar, S. N.; Mattheakis, M.; Cazeaux, P.; Narang, P.; Soljačić, M.; Kaxiras, E. *Phys. Rev. B: Condens. Matter Mater. Phys.* **2018**, *97*, 195435.
(50) Sundararaman, R.; Letchworth-Weaver, K.; Schwarz, K. A.; Gunceler, D.; Yalcin, O.; Arias, T. *SoftwareX* **2017**, *6*, 278−284.
(51) Garrity, K. F.; Bennett, J. W.; Rabe, K. M.; Vanderbilt, D. *Comput. Mater. Sci.* **2014**, *81*, 446.
(52) Perdew, J. P.; Ruzsinszky, A.; Csonka, G. I.; Vydrov, O. A.; Scuseria, G. E.; Constantin, L. A.; Zhou, X.; Burke, K. *Phys. Rev. Lett.* **2008**, *100*, 136406.
(53) Sundararaman, R.; Arias, T. A. *Phys. Rev. B: Condens. Matter Mater. Phys.* **2013**, *87*, 165122.
(54) Souza, I.; Marzari, N.; Vanderbilt, D. *Phys. Rev. B: Condens. Matter Mater. Phys.* **2001**, *65*, 035109.
(55) Giustino, F.; Cohen, M. L.; Louie, S. G. *Phys. Rev. B: Condens. Matter Mater. Phys.* **2007**, *76*, 165108.
(56) Ladstädter, F.; Hohenester, U.; Puschnig, P.; Ambrosch-Draxl, C. *Phys. Rev. B: Condens. Matter Mater. Phys.* **2004**, *70*, 235125.
(57) Gunst, T.; Markussen, T.; Stokbro, K.; Brandbyge, M. *Phys. Rev. B: Condens. Matter Mater. Phys.* **2016**, *93*, 035414.

DOI: 10.1021/acs.nanolett.8b02300
Nano Lett. 2018, 18, 5709−5715